The Astrophysical Journal, 869:60 (14pp), 2018 December 10 https://doi.org/10.3847/1538-4357/aaed2b

Magnetic Structures at the Boundary of the Closed Corona: Interpretation of S-Web Arcs

Roger B. Scott[1], David I. Pontin[1], Anthony R. Yeates[2], Peter F. Wyper[2], and Aleida K. Higginson[3]
[1] School of Science and Engineering, University of Dundee, Dundee DD1 4HN, UK; roger.b.scott@gmail.com
[2] Department of Mathematical Sciences, Durham University, Durham DH1 3LE, UK
[3] The Johns Hopkins University Applied Physics Laboratory, Laurel, MD 20723, USA
Received 2018 May 11; revised 2018 September 27; accepted 2018 October 23; published 2018 December 12

Abstract

The topology of coronal magnetic fields near the open-closed magnetic flux boundary is important to the the process of interchange reconnection, whereby plasma is exchanged between open and closed flux domains. Maps of the magnetic squashing factor in coronal field models reveal the presence of the Separatrix-Web (S-Web), a network of separatrix surfaces and quasi-separatrix layers, along which interchange reconnection is highly likely. Under certain configurations, interchange reconnection within the S-Web could potentially release coronal material from the closed magnetic field regions to high-latitude regions far from the heliospheric current sheet, where it is observed as slow solar wind. It has also been suggested that transport along the S-Web may be a possible cause for the observed large longitudinal spreads of some impulsive, ^{3}He-rich solar energetic particle events. Here, we demonstrate that certain features of the S-Web reveal structural aspects of the underlying magnetic field, specifically regarding the arcing bands of highly squashed magnetic flux observed at the outer boundary of global magnetic field models. In order for these S-Web arcs to terminate or intersect away from the helmet streamer apex, there must be a null spine line that maps a finite segment of the photospheric open-closed boundary up to a singular point in the open flux domain. We propose that this association between null spine lines and arc termination points may be used to identify locations in the heliosphere that are preferential for the appearance of solar energetic particles and plasma from the closed corona, with characteristics that may inform our understanding of interchange reconnection and the acceleration of the slow solar wind.

Key words: magnetic fields – solar wind – Sun: corona

Supporting material: animation

1. Introduction

Interchange reconnection (IR) is the process by which plasma is exchanged between open and closed flux domains (Crooker et al. 2002). Because this process by its nature occurs at the open-closed boundary (OCB), the structuring of the OCB is vitally important in determining where plasma from the magnetically closed corona will be released into the heliosphere. A significant portion of the OCB is composed of the helmet streamer boundary, which necessarily maps onto the heliospheric current sheet (HCS), suggesting that plasma that originates near the footprint of the helmet streamer would always end up near the HCS. However, Antiochos et al. (2011) showed that certain configurations of the OCB can give rise to narrow corridors of open flux that support quasi-separatrix layers (QSLs; Priest & Démoulin 1995), and these in turn map flux from very near the helmet streamer footprint to locations that are far removed from the HCS. In global models, some of these narrow corridor structures are associated with remotely observed pseudo-streamers (Wang et al. 2007), and there is growing evidence that these are linked to the slow solar wind outflow (Owens et al. 2013).

The topology of coronal magnetic fields is characterized by a complicated array of magnetic null points, their associated spine lines, and separatrix surfaces (e.g., Longcope & Parnell 2009; Platten et al. 2014; Freed et al. 2015), all of which undergo continuous dynamics. Platten et al. (2014) described various different structures that can form from combinations of separatrix surfaces, many of which are pertinent to the OCB structure. Titov et al. (2011) considered the topology of the OCB using an analytical model of an active region that forms a QSL with a nontrivial intersection with the separatrix surface of the global helmet streamer (also called the dipole streamer in Owens et al. 2014). They showed how a narrow open flux corridor with a QSL formed on a hyperbolic flux tube (HFT; Titov et al. 2002) could be transformed continuously into a genuine separatrix surface as the corridor narrows to zero width, after which a new coronal null is formed. This study highlights the importance of a holistic approach to studies of the OCB, which treats null points, separatrix surfaces, and QSLs simultaneously.

The structure and location of the OCB is directly determined by the locations of active regions, and the connection between active regions, their upflows, and IR has been explored by van Driel-Gesztelyi et al. (2012), who used spectroscopic observations from the Hinode EUV Imaging Spectrometer to infer plasma upflow velocities, which they associated with QSLs (see also Baker et al. 2017). This is consistent with the study of Brooks et al. (2015), who concluded that the majority of the slow solar wind originates near the boundaries of active regions, strengthening the argument that IR is responsible for the release of the slow solar wind (e.g., Higginson et al. 2017a). Altogether, these results support the proposition of Antiochos et al. (2011) that reconnection within the myriad separatrix surfaces and QSLs

that comprise the Separatrix-Web (S-Web) could explain the latitudinal extent of the slow solar wind (see also Crooker et al. 2012; Higginson et al. 2017b).

Reconnection at the OCB and within the S-Web may also be important in understanding impulsive, ^{3}He-rich solar energetic particle (SEP) events. Many of these impulsive SEP events are proposed to have a flare-accelerated component (e.g., Li et al. 2009; Masson et al. 2009; McCracken et al. 2012), and although the flare itself takes place in the closed corona, IR is necessary to permit the accelerated particles to access open magnetic field lines and thus escape into the heliosphere, as described by Masson et al. (2013). SEPs from single impulsive events have been observed to have spatial extents in excess of 100° longitude in the heliosphere (e.g., Wiedenbeck et al. 2013), whereas other impulsive events have much smaller spreads of ∼20° longitude or so (Reames 1999; Wibberenz & Cane 2006). It has been suggested that field line meandering may be responsible for the wide spread events (e.g., Giacalone & Jokipii 2012, and references therein). However, it is possible that the S-Web could explain the observations of both the wide and narrow events if the spread of a particular event depended on the proximity to and distribution of S-Web structures, although this idea needs further investigation.

Statistical studies of S-Web structures have been performed, but these have focused largely on solar cycle dependence. For example, Owens et al. (2014) measured the typical distribution of dipolar streamers and pseudo-streamers and showed that the latitudinal extent of the pseudo-streamer belt increases with sunspot number. Similarly, Fujiki et al. (2016) showed that the photospheric pattern of coronal hole footprints tracks closely with butterfly diagrams of the line-of-sight magnetic field.

These studies generally support the connection between active regions, the S-web, and the acceleration of the slow solar wind; however, owing to their need to span multiple solar cycles, they must rely on computationally inexpensive measures of magnetic morphology, which offer little insight into the structuring of the underlying magnetic field. In our current investigation, we endeavor to reconcile the topological and geometrical structures from empirical models with those observed in global magnetic field extrapolations. This is motivated by a need to improve our ability to recognize where these structures occur in magnetic field models from their signatures on the outermost imprint of the S-Web so that, together with studies of dynamic processes such as IR, we can improve our ability to identify locations in the heliosphere that are likely to host slow solar wind plasma and possibly impulsive SEPs.

The structure of this investigation is as follows. In Section 2 we describe our magnetic model and characterization methods. Then, in Section 3 we highlight some observed patterns in the formation of structures within the model. In Section 4 we detail some distinctions between structures formed with and without magnetic nulls present, and in Section 5 we discuss how these relate to the observed formation patterns. Finally, in Section 6 we conclude with a discussion of implications and future research.

2. Global Model

2.1. Magnetic Field

For the magnetic field model, we begin with magnetogram data from the Global Oscillation Network Group (GONG),

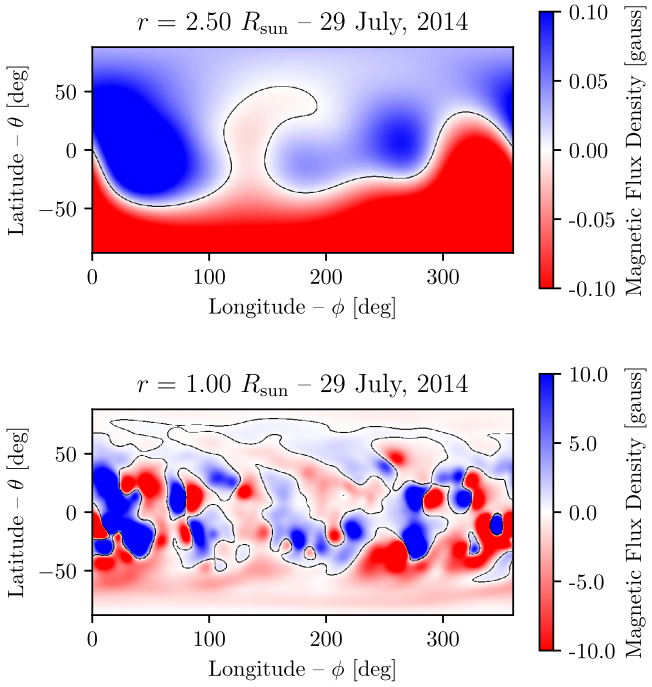

Figure 1. PFSS radial magnetic field from 2014 July 29 GONG magnetogram data, with the polarity inversion lines indicated in black. The outermost boundary (source surface) is shown in the upper panel, while the innermost boundary (photosphere) is depicted below. In the upper panel, the source surface polarity inversion line divides the positive and negative flux domains, which coincide with the predominantly unipolar northern and southern hemispheres.

which provide a synoptic measure of the full-Sun radial magnetic field at a resolution of 180 × 360 in solar sine-latitude and Carrington longitude, respectively. From the radial source data, we compute the potential field source surface (PFSS) magnetic field using a finite-difference method similar to that of van Ballegooijen et al. (2000). A `Python` implementation (Yeates 2018) of this method is available on `github`,[4] where a full description is available.

The data are smoothed by multiplying the coefficients of the spherical harmonic expansion (with harmonic degree l) by a pseudo-Gaussian filter of the form $f = \exp(-l\ (l + 1)\ k)$, with $k = 0.002$, so that the filter amplitude falls to one half at a harmonic degree of $l_{\rm f} \sim 18$. This is equivalent to allowing the source magnetogram data to diffuse for a time of 0.002 of the global diffusion time. Here, we place the outer boundary at 2.5 solar radii, and we choose a resolution of 61 × 180 × 360 in log-radius, sine-latitude, and longitude, respectively. For this investigation we focus on data from 2014 July 29; however, we have constructed 10 additional data sets, each taken on January 01, every year from 2008–2017, for a total of 11 independent magnetic models, which will be detailed in an expanded future investigation. Despite variations in the details of each model, the structures present in the 2014 July 29th data set have been found to be representative of those found in the other 10 data sets.

In Figure 1 the radial component of our model magnetic field is shown at the outer and inner radial boundaries, resampled to a resolution of 480 × 960 in colatitude and longitude for consistency with the analysis described in Section 2.2. It is worth noting that, because this model is derived from

[4] https://github.com/antyeates1983/pfss

magnetogram data taken very near the pole reversal at the maximum of solar cycle 24 (Gopalswamy et al. 2016), the northern polar region is dominated by negative flux, opposite the global dipole field. The source surface polarity inversion line is depicted by the meandering black line in the upper panel, between the predominantly red and blue hemispheres. This polarity inversion line is the base of the HCS in extended coronal models. In our PFSS model, the HCS is a null-line (since $B_\theta = B_\phi = 0$ at the source surface by construction) that sits atop a pair of separatrix surfaces that enclose the helmet streamer.

2.2. Magnetic Squashing Factor

In this investigation, we use the perpendicular magnetic squashing factor, $Q_\perp$, (Titov 2007; Pariat & Démoulin 2012) to identify regions of high complexity in the magnetic field line mapping, which we call "high-Q volumes" (HQVs). This method does not distinguish QSLs from genuine topological structures and does not explicitly determine the magnetic skeleton as would, for example, the method of Haynes & Parnell (2010). However, it has the advantage that separatrix surfaces and QSLs are identified simultaneously, each being potentially important to the process of IR.

For estimating the magnetic squashing factor, we use the `qslSquasher` code (Scott et al. 2017; Tassev & Savcheva 2017), which uses graphics processing units (GPUs) to do massively parallel field line tracing, as needed for a high-resolution volume rendering. Field line integration is performed using trilinear interpolation with an Eulerian integration step size of approximately 0.25 Mm (equivalent to 20 steps per grid cell of the source field). The output grid is $120 \times 480 \times 960$ in radius (r), north latitude (θ), and longitude (ϕ), respectively, with uniform spacing in angular coordinates and exponential spacing in the radial coordinate. Because the field line integrator must be called separately at each grid point, each instance of the global calculation corresponds to $\sim 10^8$ individual estimates of $Q_\perp$, each of which involves integration of a nine-dimensional ordinary differential equation, both forward and backward from the point of interest to the boundary. Despite the computational advantages of the `qslSquasher` routine, each global calculation requires several hours to complete on an nVidia Tesla K40 GPU, so this method is useful for studies of up to several tens of individual models, but would be ill-suited to decadal surveys of daily magnetogram models.

Because we have calculated $Q_\perp$ in a volumetric sense, we are able to identify HQVs in three dimensions and thereby infer the presence of separatrix surfaces and QSLs on the basis of their morphology. We focus primarily on HQVs that intersect the source surface, disregarding some of the more complicated QSL formations associated with twisted and braided flux tubes and sigmoid structures (e.g., Savcheva et al. 2011). Accordingly, where the HQVs have a sheetlike structure, and where $Q_\perp$ is large (but not too large), we expect the underlying field structure to resemble that of an HFT and associated QSL (see Figure 7 of Titov et al. 2011 and Figures 3 and 4 of Antiochos et al. 2011). Where $Q_\perp$ is very large (formally infinite), we expect there to be a magnetic null and an associated separatrix surface. And, in addition, where $Q_\perp$ is discontinuous, we expect there to be a bald patch and an associated separatrix surface (Titov 2007). Furthermore, the separatrix surface associated with the three-dimensional (3D) OCB can be identified as the interface between open and closed magnetic flux domains, and although the footpoint locations of individual field lines are not retained by `qslSquasher`, this information is encoded into the value of $\mathrm{slog}_{10} Q_\perp = \pm \log_{10} Q_\perp$, which we define to be positive (negative) if the associated field line is closed (open).

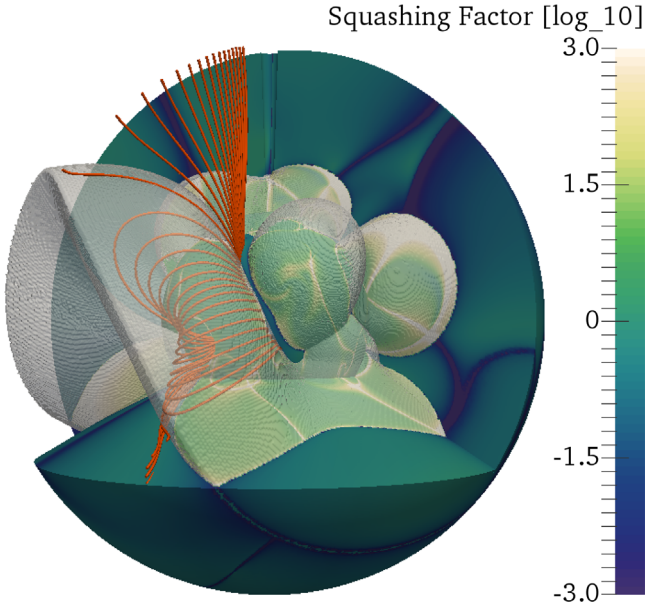

Figure 2. 3D rendering of the signed magnetic squashing factor ($\mathrm{slog}_{10} Q_\perp$) with representative magnetic field lines (orange). Cuts of constant radius ($r/R_{\mathrm{Sun}} = 1.0, 2.5$), latitude ($\theta = -30°$), and longitude ($\phi = 90°, 270°$) show the volumetric nature of the calculation, while the translucent white surface depicts the OCB. As the figure rotates, the $r = 2.5\,R_{\mathrm{Sun}}$ coordinate slice becomes transparent to show the position and shape of the OCB relative to the HCS, which forms along the apex of the helmet streamer.

(An animation of this figure is available.)

In the animated Figure 2, $\mathrm{slog}_{10} Q_\perp$ is depicted by the color map so that green regions have relatively low $Q_\perp$, whereas regions of large $Q_\perp$ are either bright yellow or dark violet, depending on whether the flux is closed or open. The OCB is represented by the translucent white surface,[5] whose intersection with the $r = 2.5\,R_{\mathrm{Sun}}$ coordinate slice defines the location of the HCS. The portion of the OCB that connects up to the HCS defines the boundary of the helmet streamer, which encloses the majority of closed coronal flux. Outside the helmet streamer, smaller closed flux domains are visible as dome-shaped structures embedded within the larger open flux domains.

Although a 3D rendering is useful for providing context, recognizing coronal structures, and informing our intuition for the shape of the various flux domains, it is convenient to visualize the calculation in the native polar coordinates of the spherical domain. In Figure 3 the angular dependence of $\mathrm{slog}_{10} Q_\perp$ is depicted for a selection of constant-radius slices, from just inside the source surface, down to the photosphere. The position of the outermost slice (just below the source surface at $r = 2.5\,R_{\mathrm{Sun}}$) is chosen to allow for some closed flux to be visible (thereby indicating the position of the HCS), which is not possible at the source surface, where all flux is open by construction. Notice that the shape of the HCS in the top left panel corresponds to the HCS contour shown on the

[5] Because the squashing factor along the OCB is formally given by $\mathrm{slog}_{10} Q_\perp = \pm\infty$, depending on whether it is approached from the open or closed field, it is represented here as an isosurface of $\mathrm{slog}_{10} Q_\perp = 0$.

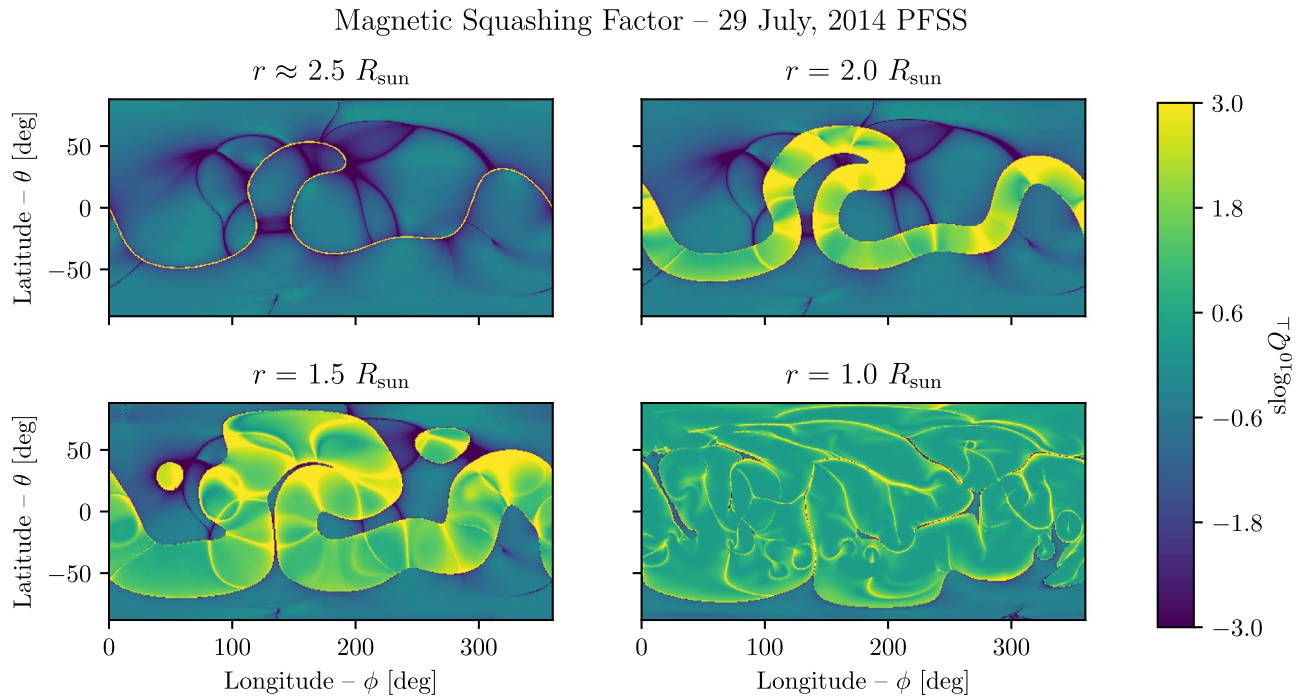

Figure 3. Color map of $\mathrm{slog}_{10}Q_\perp$ at radial positions of $r/R_{\rm Sun} = \{1.0, 1.5, 2.0, 2.5\}$ for the 2014 July 29 PFSS model. Positive (negative) values indicate closed (open) flux. Dark bands at the upper boundary indicate the intersections of high-Q volumes with the source surface. The presence of separatrix surfaces that divide open and closed flux can be inferred from the abrupt transitions in color and brightness.

outer surface in Figure 2, and that in regions where the inside of the volume is visible in Figure 2 this also corresponds to the top of the 3D helmet streamer.

3. Observed S-Web Structures

We have previously established the convention that regions of sufficiently high $Q_\perp$ ($\gtrsim 10^{3.5}$ in our model) are labeled HQVs, and these may, in fact, be either QSLs or separatrix surfaces, depending on the presence of magnetic nulls or bald patches. The combined network of all HQVs is understood to form the S-Web (Antiochos et al. 2011), which is here taken to be a 3D structure. The outermost imprint of the S-Web can be seen in the map of $\mathrm{slog}_{10}Q_\perp$ at the source surface (i.e., the entire structure visible in the top left panel of Figure 3).

The most prominent HQV in the S-Web is associated with the helmet streamer, whose apex lies along the HCS[6] and traces the radial outer limit of the OCB (see Figure 2). Away from the HCS, in the unipolar open flux domains, HQVs often intersect the source surface along elongated, quasi-one-dimensional bands of highly squashed flux, which we call "high-Q arcs" (HQAs), seen as the purple bands connected to the HCS in the top left panel of Figure 3. These HQAs shall be the focus of this investigation, for which the main line of inquiry is the following: Can we rigorously differentiate between the kinds of structures that form HQAs of various levels of complexity, and, if so, what does this tell us about the underlying coronal magnetic field?

To proceed, we must establish some terminology for describing portions of the S-Web, on the basis of how the observed HQAs connect to each other and to the HCS. In the following sections, we shall use the term "vertex" to describe the intersection of multiple HQAs away from the HCS. The sections of HQAs between vertices and/or intersection with the HCS are called "segments," and these are typically bounded at both ends by either a vertex or HCS intersection, but can in some cases end abruptly, away from any other HQA structures. In order that vertices should be defined unambiguously, we require that for segments to join at a vertex there must be at least one sharp angle of intersection—that is, a single smooth arc cannot be arbitrarily divided into a pair of segments and a vertex. We shall further divide HQA segments into three subclasses, which are discussed below.

3.1. Simple Arc Segments

First, we consider HQA segments that connect to the HCS at both ends and have no other intersections, and these we call "simple segments." Simple HQA segments are ubiquitous in the model, and we have indicated two examples in Figure 4. In the figure, the HCS exhibits an obvious excursion to high latitude at $\phi \approx 130°$. If we consider a closed curve composed of this northerly excursion of the HCS and the HQA labeled "simple segment 1," this curve encloses a unipolar negative flux domain that extends into the northern hemisphere. Within this domain, there is another simple HQA segment, labeled "simple segment 2," which encloses a smaller subset of the same flux. Because all of the flux at the source surface is open, each of these flux domains corresponds to a coronal hole, which is separated from the rest of the open flux domains by the structures underlying the HQAs. We refer to the smaller flux domain as being "embedded" within the larger, and the associated simple arc segments are said to be "nested."

Looking at the bottom and left side panels of Figure 4, we see slices through the 3D domain at constant $\theta \approx -30°$ and $\phi \approx 140°$, corresponding to the dashed lines on the main panel. The closed-field regions are shown in yellow-to-green, whereas

[6] In some models the HCS may be composed of multiple disconnected curves, each with its own helmet streamer.

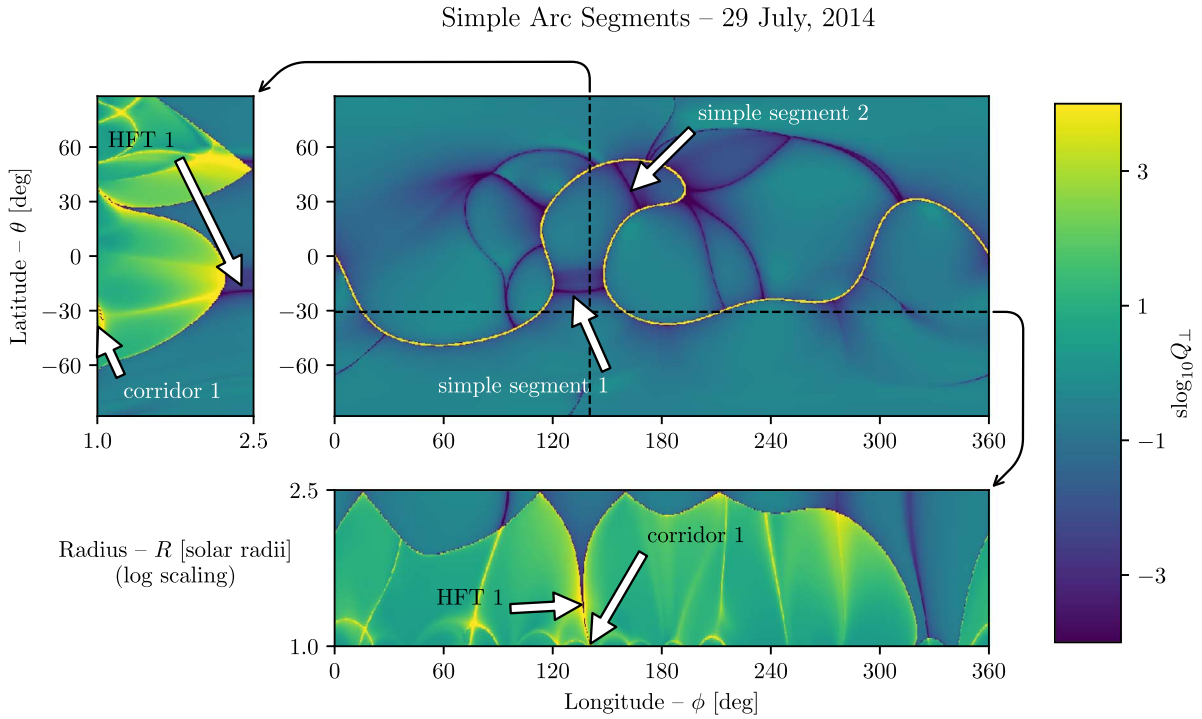

Figure 4. Simple arc segments at $r \approx 2.5\ R_{\rm Sun}$ (source surface). Cross sections through $\theta \approx -30°$ and $\phi \approx 140°$ show the 3D structure of a high-Q volume that maps down to a narrow corridor, which is bounded by the OCB on either side.

the open field regions are shown in green-to-violet. The locations where the closed field regions extend to 2.5 solar radii in each of the side panels are locations where the top of the helmet streamer and its connection to the HCS are sampled. Closed field regions that do not extend all the way to 2.5 solar radii may still be associated with the helmet streamer, but may be places where the chosen cross sections slice across its flank.

From these cross sections, it is apparent that the HQA labeled "simple segment 1" is the outermost footprint of an HQV that extends down through the volume and eventually connects to an open flux corridor on the photosphere. Accordingly, we identify this as an HFT, though it may in fact contain nulls at very low heights above the photosphere. This structure can also be seen by following the HQVs of the two simple segments down through the volume in Figure 3, where we find that, as more of each radial slice is taken up with closed field beneath the helmet streamer, the simple segments contract along their length and expand along their width. These eventually thin to narrow corridors of open flux at the photosphere, which connect a series of small coronal holes that extend from the southern polar crown into the predominantly closed midlatitude region.

The tendency of simple arc segments to be associated with seemingly simple HQVs that are morphologically similar to HFTs is a generic feature in the model. Moreover, where these intersect the helmet streamer, we invariably observe a continuation of the same HQV into the closed field region. This suggests that, whatever magnetic structure is responsible for the formation of a simple arc segment, it is not isolated to the open field but is, in fact, part of a larger structure that spans the OCB. This has important implications for the slow solar wind. Any IR process that may take place on such a portion of the OCB now also shares connections to magnetic structures (often associated with active regions) that extend into the closed field regions, where the plasma properties can vary substantially (Parenti et al. 2017).

3.2. Branching Arc Segments

In contrast to simple segments, which have exactly two points of intersection with the HCS and no other intersections, we refer to "branching segments" as HQA segments that intersect each other at a vertex, away from the HCS. The most common type of branching segment exhibits a single intersection with the HCS and a single vertex intersection that is shared by (typically two) other branching segments. There are also examples of branching segments that have no intersection with the HCS but connect instead to a vertex at each end. Branching segments that connect twice to the same vertex may exist but have not been observed.

Several examples of branching segments are given in Figure 5, which shows two vertices, labeled "vertex 1" and "vertex 2," each of which is located at the intersection of three branching segments, labeled "segment 1a," "segment 1b," and so forth. In the case of "vertex 1," the segment labeled "1a" appears to be formed of two merged segments, so this branching system may involve four segments, rather than three. In the case of "vertex 2," the segment labeled "2c" appears to merge with a simple segment farther to the south, but this may be a case of a branching segment joining two vertices. Variations of this kind from one branching system to the next are common, but do not appear to materially affect the structure of the S-Web near the vertices.

Referring again to Figure 5, we note that, where simple segments have been observed to occur on the concave side of HCS excursions, these branching segments tend to occur on the convex side of the HCS, and this has been found to be generally true for the other models that we have considered. Furthermore, inspecting the bottom and left panels in Figure 5, it is apparent that, although the simple segments tend to be associated with HFTs and narrow corridors, the HQVs associated with branching segments tend to map down to

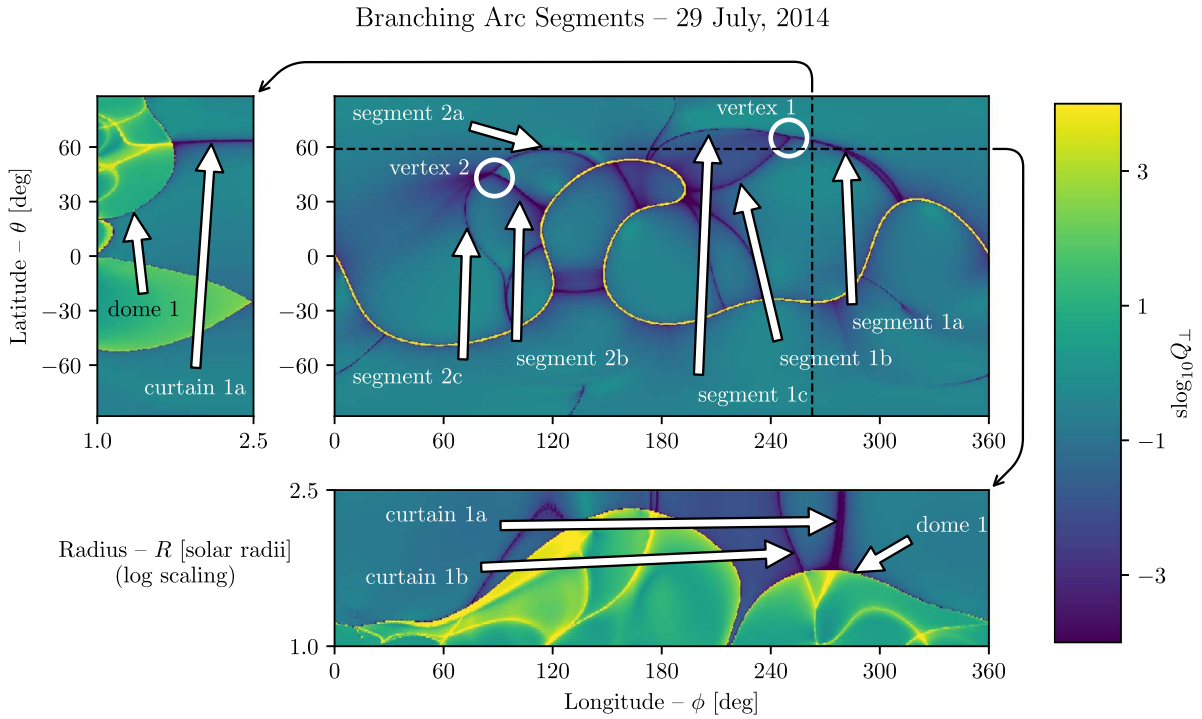

Figure 5. Group of branching segments at the $r = 2.5\ R_{\rm Sun}$ surface (source surface). Cross sections through $\theta \approx 60°$ and $\phi \approx 260°$ show the 3D structure of a high-Q volume that maps to a separatrix dome whose apex is at $r \approx 1.75\ R_{\rm Sun}$.

dome-shaped closed field regions, leading us to infer that these may support large-scale topological structures, rather than HFTs. In the figure, the HQVs that connect to the vertices have been labeled as "curtains," owing to their morphological similarity to the separatrix fan curtains described in Titov et al. (2011), and especially those depicted in Figures 3, 4, and 5 of Platten et al. (2014). The association between vertices and separatrix dome structures can also be seen in Figure 3, in which both of the mentioned vertices can be traced down to small ellipsoidal patches of closed flux in the bottom-left panel, these being near the apices of closed field separatrix domes.

3.3. Detached Arc Segments

Finally, we address detached segments, which are HQAs with at least one free end that terminates away from any other S-Web structure. These are referred to as "partially detached," in cases where the segment has one intersection and one free end, or "fully detached," in cases where the segment has two free ends and no intersections. In principle, a partially detached segment could join a branching group at a vertex; however, this has not been observed. Detached segments appear far less commonly than do simple or branching segments; nonetheless, these structures are generic features, and, as we shall see, they are critical to our overall understanding of HQA formation.

There are three examples of detached segments in our global model. One of these is in the northern hemisphere, at $\phi \approx 180°$, and extends from the HCS to the northern pole. Another is in the southern hemisphere, at $\phi \approx 130°$, and exhibits a similar polar connection but forms no connection with the HCS. Both of these detections are considered unreliable because they involve field line integration through the polar region, where the model magnetic field is poorly constrained.

The third example is indicated in Figure 6 and exhibits one connection to the HCS, extending southwest from there and terminating abruptly at $(\theta,\ \phi) \approx (-30°,\ 320°)$, with no other intersections. Like the branching segments previously discussed, the HQV associated with this detached segment also forms a "curtain," which is morphologically similar to the configuration in Figure 4 of Platten et al. (2014), intersecting the helmet streamer at one end and terminating above the apex of a closed field separatrix dome in the low corona. Examples from other models show a similar tendency, with the termination point typically mapping down onto a closed field separatrix dome, which is usually smaller than for branching segments, and typically occurs at lower heights in the corona. Because there are so few examples of detached segments, it is difficult to say whether these form preferentially on the concave or convex side of the HCS, although we can say that no nested examples have been observed.

3.4. Summary of Observed Structures

In summary, we have developed a scheme for categorizing the manner in which HQA segments intersect the HCS and each other, and we find that this can be an indicator of the structure of the interior of the domain. In particular, where the HCS has a large excursion away from midlatitude, the concave side of the HCS, which corresponds to the intrusion of open flux into the opposite-signed hemisphere, typically supports simple arc segments, which are morphologically similar to HFTs that map to narrow corridors of open flux at the photosphere. Conversely, the convex side of the HCS, which corresponds to the flux that has been deformed away from midlatitude to accommodate the deformation of the helmet streamer, typically supports branching arc segments, which intersect at vertices away from the HCS and typically connect to closed field separatrix dome structures lower down in the

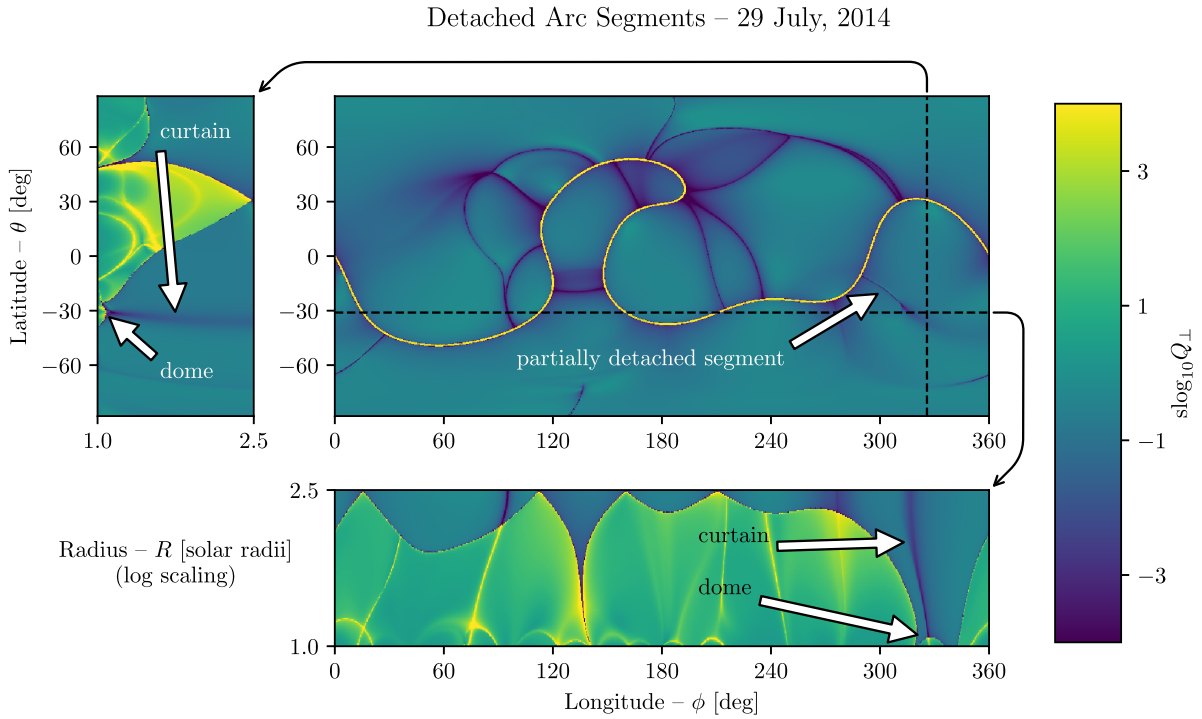

Figure 6. Partially detached segment at the $r = 2.5\ R_{\rm Sun}$ surface (source surface). The segment exhibits only one intersection and terminates away from the HCS. Cross sections through $\theta \approx -30°$ and $\phi \approx 320°$ show the 3D structure of a high-Q volume that maps to a separatrix dome whose apex is at $r \approx 1.1\ R_{\rm Sun}$.

coronal volume. Detached segments, which occur less frequently than other segment types, seem to share structural similarities to branching segments, in that they also tend to be associated with low-lying, closed field separatrix dome structures.

4. Theoretical Interpretation

Although the associations made in the previous section are plausible, the analysis lacks rigor—we have drawn heavily on visual comparisons to theoretical studies of separatrix surface topologies and analytical field models, but we have not constructed a magnetic skeleton, so our only well-defined topological feature is the OCB. We now focus on the formation of such structures from a theoretical perspective, by considering the field lines that form the OCB and how these map between the photosphere and the source surface.

4.1. Narrow Corridors: Simple Arc Segments

We first consider the simplest configuration that can create an HQV with an imprint at the source surface: a QSL formed from an HFT along the OCB. Antiochos et al. (2011) described just such a configuration in which a portion of the OCB associated with the HCS passes near to itself, creating an isolated coronal hole that remains connected to the larger region of open flux through a narrow corridor of open flux, which is bounded on either side by the closed flux beneath the helmet streamer. We assume that apart from this feature the magnetic field is the simple global dipole field and that the OCB footprint is formed of a pair of simple closed curves, one in each magnetic polarity, which are the photospheric footprints of the helmet streamer boundary. A depiction of this configuration is shown in Figure 7 (see also Figure 1 of Antiochos et al. 2011). Field lines map the OCB footprint to the HCS in a one-to-one fashion that preserves the ordering of field

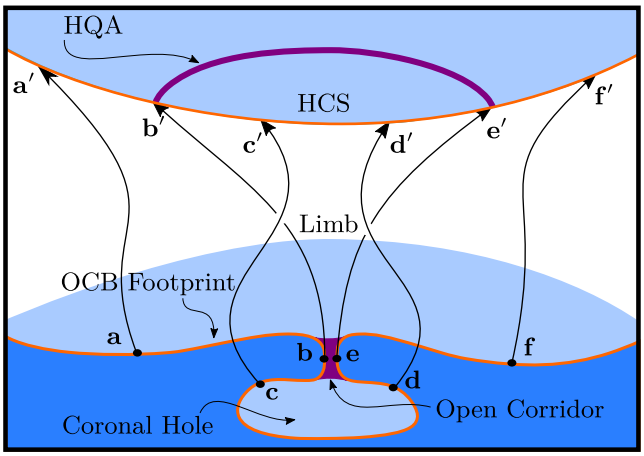

Figure 7. Diagram of a high-Q arc formed by a narrow corridor. The orange curves represent the HCS and the (northern) photospheric footprint of the OCB, which divides open flux (light blue) from closed (dark blue). The mapping preserves the ordering of points along the two curves.

line footpoints (mathematically, the HCS is diffemorphic to each of the OCB footprints, and the mapping of open field lines is smooth and bijective in either polarity), this being critical for the following analysis.

Consider the example shown in Figure 7. A narrow corridor and the corresponding HQA are shown in purple, while the OCB footprint and HCS are indicated in orange. Positive flux is shown in blue, with the lighter and darker shades indicating the open and closed field, respectively. Points $\boldsymbol{b}$ and $\boldsymbol{e}$ on either side of the narrow corridor must map to points $\boldsymbol{b}'$ and $\boldsymbol{e}'$ on the HCS, which are on either side of $\boldsymbol{c}'$ and $\boldsymbol{d}'$, to preserve the ordering of the mapping. In addition, the flux from within the narrow corridor must connect between $\boldsymbol{b}'$ and $\boldsymbol{e}'$ at the source surface and, moreover, must enclose all of the flux from the isolated

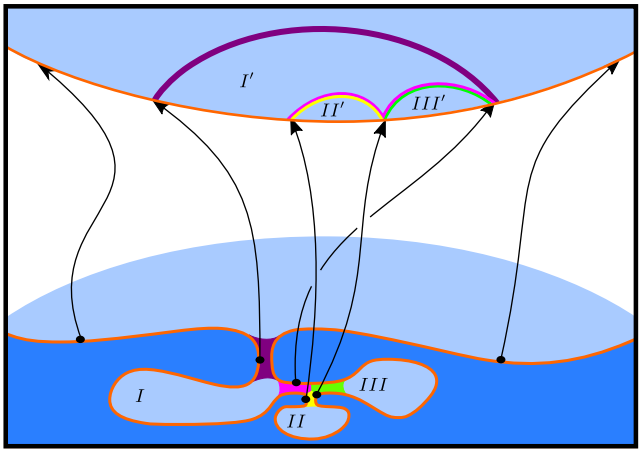

Figure 8. Depiction of multiple coronal holes linked in a system of narrow corridors. Each corridor (colored purple, magenta, yellow, and lime green) creates a high-Q arc (with the same color coding). Depending on the configuration, these can be nested or adjacent, with distinct or shared intersections with the HCS. In all cases, the high-Q arcs form simple arcs segments.

coronal hole. Accordingly, the corridor flux must be stretched out to form the magenta HQA shown in the figure at the top boundary. Note that the magnitude of $Q_\perp$ within a given arc is largely determined by the aspect ratio of the HFT within the corridor, whereas the amount of flux within the arc is determined by the area and typical field strength within the corridor. It follows then that longer corridors tend to have thicker arcs (for a given value of $Q_\perp$), whereas wider corridors tend to have lower values of $Q_\perp$ (for a given total flux).

The stretching of the corridor flux between the two high-aspect ratio footpoints is consistent with an HFT (Titov et al. 2002), and, by construction, an HFT that spans an open flux corridor must create an HQA that intersects the HCS at both ends (although the HFT itself is not bounded by the OCB but will extend into the closed field adjacent to the corridor). We submit that, by extension, any configuration of linked corridors and their corresponding HFTs will create a network of multiple HQAs, all of which connect twice to the HCS. These may merge, and share common points of intersection with the HCS, or may nest, so that larger coronal holes contain HQAs that subdivide the region into smaller coronal holes, but the assertion is that no vertices will be formed away from the HCS.

To support this claim, we have illustrated a complex corridor system in Figure 8, which contains a generic combination of HQAs, resulting from corridors that link coronal hole domains in parallel or sequential order. As in Figure 7, the OCB (in the polarity shown) is a single, continuous curve, and it must map to the HCS in a way that preserves the ordering of field line footpoints. Additionally, the open photospheric flux domains labeled *I*, *II*, and *III* map to domains *I*′, *II*′, and *III*′ at the source surface.

Because points along either side of the purple corridor are the limits of a line element containing points along either side of the other three corridors, the corresponding HQAs from these latter three must be nested within the former. Coronal holes *II* and *III* are connected in parallel to *I* (via the yellow and lime green corridors), and these together are connected in series (via the magenta corridor) with the polar coronal hole (not labeled). Thus, the open flux domains *II*′ and *III*′ are adjacent to each other and are embedded within *I*′.

And because the purple corridor is adjacent to the magenta at one end, the corresponding HQAs appear to merge at one end, forming a common intersection with the HCS. The yellow and lime green corridors are similarly adjacent at the photosphere, and their HQAs share a common point of intersection with the HCS as well, though they are adjacent rather than nested. More subtle is the position of the magenta HQA—the magenta corridor contains only flux from domains *II* and *III*, so the corresponding HQA can only enclose domains *II*′ and *III*′. The magenta corridor is effectively a shared "upstream" corridor region that maps to a double-humped structure that hugs the top of the yellow and lime green HQAs, thickening each but not changing their general shape.

The construction in Figure 8 is intended to be an extreme example, which is more complex than is typically observed in the coronal magnetic field extrapolations that we have considered. Nonetheless, this example serves to illustrate that, for any configuration in which the photospheric OCB footprint forms a simple closed curve—irrespective of its geometrical complexity—the resulting HFTs cannot form HQA vertices away from the HCS. To understand how vertices of HQAs are formed, we must consider structures that map segments of the OCB into unipolar, open flux domains, away from the HCS, which necessitates that there should be some singular behavior in the mapping, and this leads to the consideration of magnetic nulls.

4.2. Narrow Corridors: Detached Arc Segments

A survey of magnetic null topologies in global models was previously performed by Platten et al. (2014), who considered various configurations of coronal nulls and separatrix surfaces. The simplest of these structures is a so-called separatrix dome, which is a closed separatrix surface that is formed when a coronal null exhibits a fan (separatrix) surface that curves down on all sides and intersects the photosphere along a simple closed curve (see Figure 2 of Platten et al. 2014). Underneath, and completely enclosed by the dome, there must exist a patch of parasitic polarity flux, which closes down locally, necessitating a separatrix surface to divide it from the surrounding flux, which maps to a more distant region. Reconnection at these generic structures in general permits an exchange of plasma/magnetic flux between the inside and outside of the dome (Pontin et al. 2007, 2013) and has been invoked to explain a range of energetic coronal events.

The field line mapping in a magnetic dome topology with a single null is such that any point along the footprint of the dome maps to the null point, and from there to the footpoints of the null spine line. The "inner spine" footpoint lies in the parasitic polarity, whereas the "outer spine" footpoint can be either open or closed, depending on the nature of the surrounding flux. If the outer spine line is open, then the dome separates open flux from closed and must comprise a portion of the OCB, which is necessarily disconnected from the larger portion of the OCB that is formed by the helmet streamer (see Figure 9). The entirety of this detached segment of the OCB maps to a single point, the null spine footpoint, which terminates somewhere in the open flux region, away from the HCS (mathematically, the presence of a null separatrix dome induces a surjection in the local mapping). It follows, therefore, that if an HQV is formed adjacent to a separatrix dome with an open spine line, then one end of the corresponding HQA will

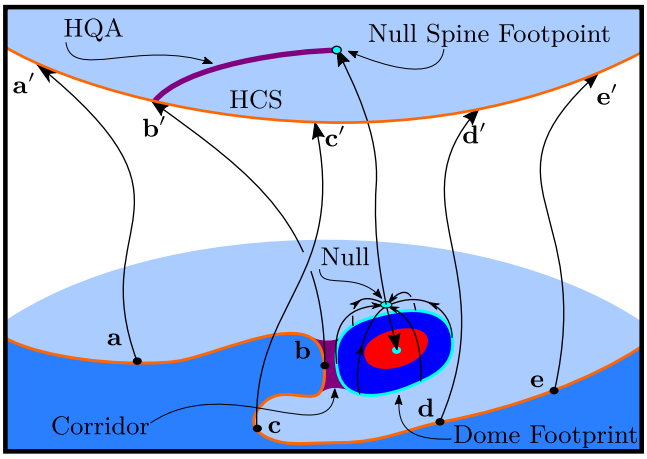

Figure 9. QSL formed in a narrow corridor where the main OCB is brought close to a null separatrix dome footprint (cyan), formed above a parasitic polarity region (red oval) in an otherwise open coronal hole. An HFT is formed, which extends from the corridor to a high-Q arc at the source surface; however, because the null spine is not positioned along the HCS, the high-Q arc terminates abruptly in the open field region.

terminate at the null spine line footpoint, away from the HCS, as shown in Figure 9.

This consideration for the portion of the OCB that corresponds to the footprint of null fan surfaces is critical to our understanding of HQAs. Because the fan surface footprint forms a nonzero portion of the OCB, separate from the helmet streamer, that is mapped to a point *away from* the HCS, these structures allow narrow corridors of open flux to be bounded on both sides by regions of closed flux, without requiring that the corresponding HQA have two intersections with the HCS. The configuration described above and depicted in Figure 9 provides a plausible explanation for the detached segments described in Section 3.3 and depicted in Figure 6, and this provides a key element for our understanding of more complicated structures.

4.3. Corridors of Zero Width

The inclusion of magnetic nulls in the model is not difficult to motivate, as it has been shown that coronal nulls are generic and ubiquitous, especially in the low corona (Cook et al. 2009; Longcope & Parnell 2009; Edwards & Parnell 2015; Freed et al. 2015). By allowing for an isolated coronal null in the open field region, we have demonstrated the formation of detached HQA segments as described in Section 3.3, which is consistent with our observation that these structures are typically associated with low-lying, closed field dome structures that are embedded in the larger open field region.

Similar closed field dome structures are also observed within the larger closed field region beneath the helmet streamer and adjacent to open flux corridors. Referring to the bottom-left panel of Figure 3, we see that, adjacent to the apex of the closed dome structure at $(\theta, \phi) \approx (30^\circ, 50^\circ)$, there is an ellipsoidal dome structure (closed curve of high $Q_\perp$) within the closed flux region underlying the helmet streamer and centered at $(\theta, \phi) \approx (10^\circ, 90^\circ)$, which causes the OCB footprint to bulge into the open field region. As it happens, this is a rather generic feature, with corridors commonly forming in regions where separatrix dome structures in adjacent closed field domains press toward one another, pinching the open flux between them. It is natural, therefore, to consider whether a collection of such null domes could form a more complicated topology that would exhibit the same morphological signatures as an HFT arising from a narrow corridor. Indeed, Platten et al. (2014) have described a host of other topological structures that can form nontrivial intersections with the OCB.

Here we have elected to explore the interaction of a pair of separatrix domes, which are brought progressively closer together, so that the corridor between them is made progressively narrower, to the point of having zero width. This was done using an analytical potential field model involving a pair of submerged monopoles and a uniform background field. Our findings are illustrated in Figure 10 in which we show two configurations with nearly identical flux distributions that both create a small coronal hole, which is separated from the majority open flux domain by either a narrow corridor or a separatrix surface, depending on the details of the local magnetic field.

In the top panel of Figure 10 the magenta field line in the center represents open flux, which is bounded on either side by the OCB of the helmet streamer (orange field lines). There are two nulls in the closed field region (labeled N_a and N_b and colored cyan and lime green, respectively), which form above the red parasitic polarity patches, deforming the OCB footprint (orange curve), and an HFT maps flux from the narrow corridor (purple) up to an HQA (represented by the purple over-bar), similar to Figure 7. If, however, the corridor is narrowed to zero width, either due to motion of the parasitic polarity regions or due to changes in the large-scale field, then a new pair of nulls (of opposite type and zero combined topological index) can form within the corridor via a saddle-node bifurcation[7] (Priest et al. 1996). These nulls do not rise through the photosphere but are born in the corona, and their presence leads to a configuration like the one shown in the bottom panel of Figure 10, in which the HFT of the previous example has been replaced by a pair of intersecting separatrix fan surfaces from the two central nulls (labeled N_c and N_d and colored yellow and dark green, respectively).

The fan surface of N_c maps up to the HQA formerly associated with the corridor HFT and intersects the OCB along the orange field lines. It is bounded by the spine lines of the preexisting nulls (N_a and N_b), making it a "curtain" that spans from the closed field, across the open field, and back into the closed field again. The fan surfaces of N_a and N_b intersect the fan surface of N_c along separator field lines (dashed white overlay), and together these surfaces form a single separatrix dome.

Because the spine lines of N_a and N_b are closed, the triple-null dome is entirely in the closed field, *except* along the spines lines of N_c (yellow dashed overlay), which form an "archway" that "bridges" the photospheric region previously associated with the narrow corridor. The spines of N_c form a portion of the helmet streamer and thus map to a pair of points on the OCB footprint, which no longer form an ordered pair but are the only points of intersection between the footprints of the OCB and the null dome separatrix surface. The coronal hole that is formed in this case is, therefore, now connected to the majority flux domain only through the spine lines of N_c, making it *linked but not connected*, much like the configuration described in Titov et al. (2011).

[7] Other variations that arise from similar source configurations include the merging of the upper nulls via the reverse of either a pitchfork or saddle-node bifurcation, but these are less relevant to the discussion of HQAs.

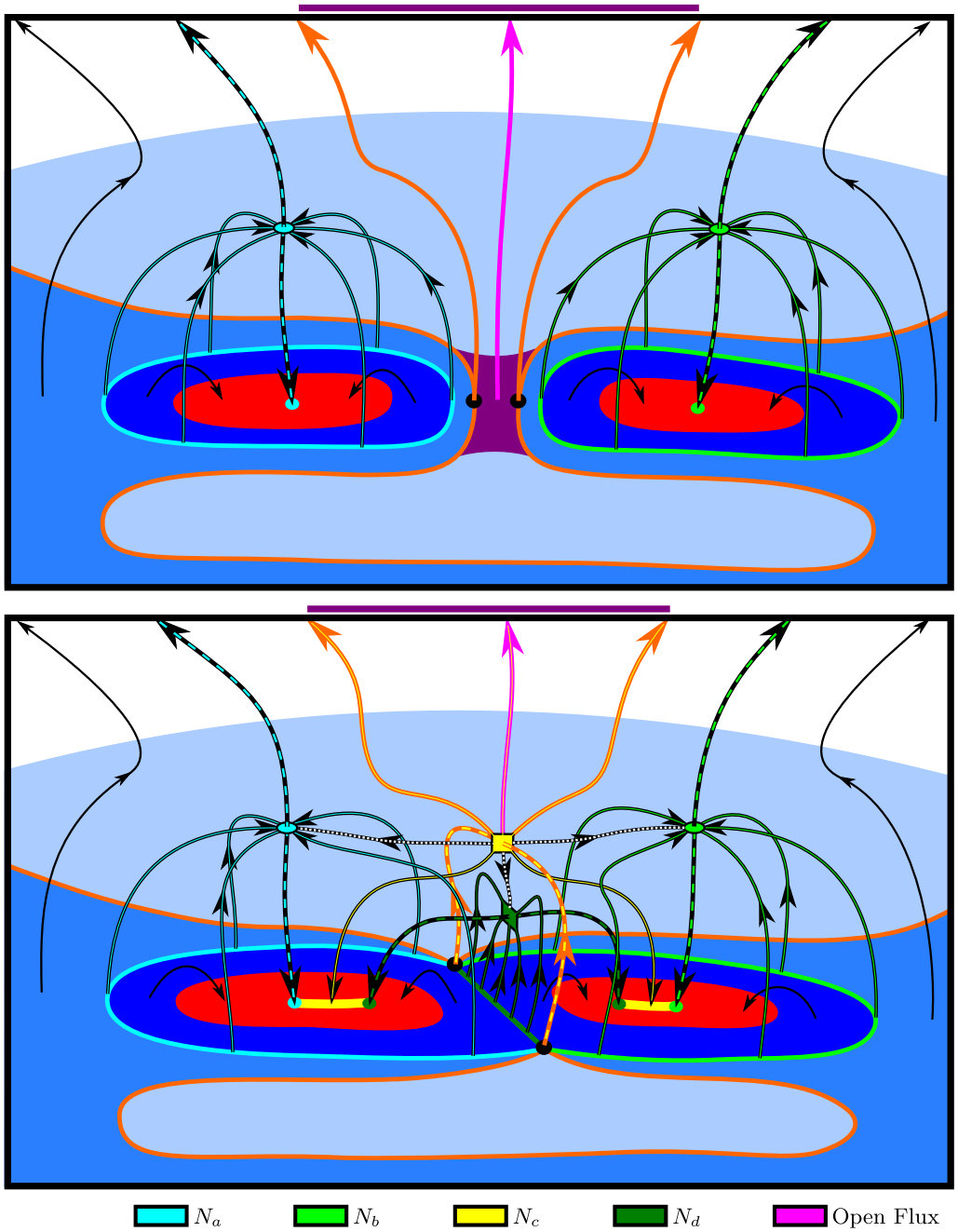

Figure 10. Diagram of zero-width corridor. The OCB footprint (orange curve) maps down from the HCS (not shown) along the orange field lines. Black field lines represent closed flux. Field lines with color overlay map to magnetic nulls of the same color coding, with dashed overlay indicating spine lines and solid overlay indicating fan field lines. Separatrix surfaces and spine footpoints are color coded according to their respective nulls. Dark blue and red regions indicate positive and negative flux within the null separatrix domes. In the top panel, there are only two nulls, each within the closed field region, and the smaller coronal hole remains connected to the larger via an open flux corridor. In the bottom panel, the open flux of the corridor is replaced by a pair of nulls and their fan surface field lines. The coronal holes are now *linked but not connected*.

The presence of the lower central null (N_d) is required by the separation of the two parasitic polarities; the fan surface of N_c cannot intersect a photospheric polarity inversion line except at a bald patch. If the parasitic polarity regions are merged (e.g., due to flux cancellation), the orange null submerges, leaving a simpler triple-null system. Moreover, if the parasitic polarity regions merge with the majority negative polarity region in the southern hemisphere, then N_a and N_b are no longer strictly required; topologically, it is only the presence of N_c and N_d that is required to allow the OCB to collapse onto itself while preserving the flux distribution within the corridor region. Thus, it may be possible for the corridor width to collapse to zero without the presence of the null dome structures in the closed field; however, this is conjecture as we have not shown this explicitly in our analytical model.

All of these states are dynamically connected through a sequence of potential fields; however, the details are strongly dependent on the model parameters, especially the symmetry of the source configuration. Moreover, the construction that we have described, arising from the spontaneous formation of nulls, is only one way of forming a triple-null dome whose fan surface spans the OCB. Another way would be to begin with a

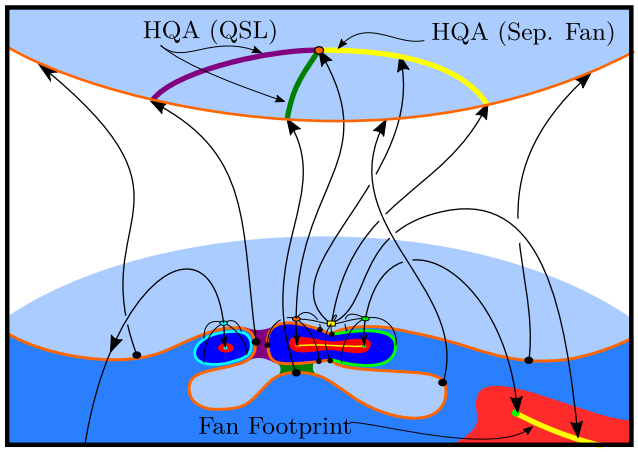

Figure 11. System of high-Q arcs formed from a combination of corridors of various width, with a vertex at the spine line of a magnetic null in the open field. Three arc segments meet at the vertex, two being formed from HFTs, and a third being the footprint of a separatrix "curtain" from a triple-null system that spans the OCB.

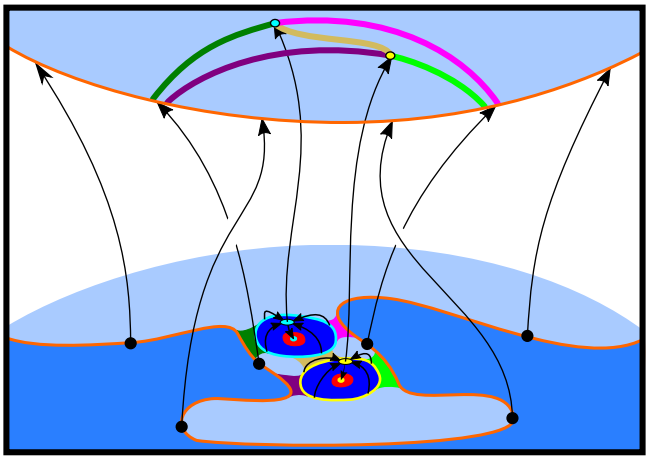

Figure 12. Collection of null dome structures within a corridor. The larger corridor is made up of a number of smaller corridors that form between adjacent sections of the OCB footprint, creating arcs that attach vertex-to-vertex. With increased resolution (in either the model or the rendering of $Q_{\perp}$) a network of similar such features may be visible within seemingly simple HQAs.

triple-null system where both vertical spines are embedded in the same closed field region and then to let one spine line open across the OCB, migrate across the corridor, and then close down across the opposing portion of the OCB (e.g., Titov et al. 2011). It is enough to know that both configurations depicted in Figure 10 are generic and are likely present in the corona on some scale at all times.

4.4. Systems of Corridors: Branching Arc Segments

Allowing for the inclusion of nulls with spine lines in the open field, as well as linked coronal holes separated by multi-null separatrix domes, we have established the key ingredients underlying the formation of HQVs in the S-Web. In Figure 9 we showed how a single arc could terminate away from the HCS, but given that a single separatrix dome footprint can form multiple corridors with different portions of the OCB, it is clear that multiple HQAs can all terminate at a single spine line, creating a vertex as described in Section 3.2. Furthermore, by considering the merging of closed field domains across an open corridor, we have seen that these can vanish to zero width, ultimately becoming separatrix surfaces, which leads us to conclude that the distinction between QSLs and separatrix surfaces in the S-Web is largely a matter of limiting cases, particularly in the case of simple arc segments.

With these considerations in mind, we can now consider a generic configuration involving an ensemble of the various structures that we have described, as shown in Figure 11. In the figure, the OCB footprint is again a single line; however, the triple-null system, which has one open outer spine (orange) and one closed (lime green), has created a "singular segment" along the footprint of the helmet streamer (i.e., a segment that maps to the single footpoint of the open field null spine line, away from the HCS). The two narrow corridors, in purple and dark green, form an HQA vertex at the null spine line, where a third HQA segment, formed from the fan curtain of the central null, completes the triple arc system.

This is only a representative example. Either of the two corridors could also pinch off to create a fully detached (but linked) coronal hole. We note that the formation of this singular segment of the OCB along the footprint of the helmet streamer is critically dependent on the presence of a multi-null dome structure that spans the OCB, with at least one closed spine and one open spine; because the intersection of a spine with a separatrix is topologically unstable, any single-null dome must be embedded either entirely in the open field or entirely in the closed field, away from the helmet streamer boundary, as demonstrated by Edmondson et al. (2010).

We also note that, although the triple-null dome contributes to the complexity of this example (allowing one of the HQAs to be a genuine separatrix footprint), it is the presence of the open field spine line, and not the complexity of the dome to which it attaches, that allows for the formation of a vertex away from the HCS. This is easily seen by considering another example, consisting not of a complex null dome structure that spans the OCB, but rather of a pair of simple null dome structures that exist within a larger corridor of otherwise open flux. Such a configuration is depicted in Figure 12, in which a narrow corridor, that would otherwise be bounded by a continuous OCB footprint, is complicated by a pair of parasitic polarity regions. The corridor flux is broken up between five smaller corridors, each of which is bounded by closed flux within the low-lying null dome structures.

Each of the associated HQAs is of the branching type, with the dark green, magenta, and beige sharing a vertex at the spine line of the cyan null, while the lime green, purple, and beige share a vertex at the spine line of the yellow null. The beige segment, in particular, is noteworthy in that it connects the vertices of two separate null spine lines, whereas the other four segments each connect from a single vertex back to the HCS. Structures such as this could be difficult to detect in lower resolution renderings, but may be ubiquitous given the number nulls occurring just above the photosphere. For the slow solar wind, arrangements of this type allow for the possibility of even more plasma escape from the closed field regions, and if the S-Web affects the spread of impulsive SEPs, then large-scale structures such as these may have an appreciable impact. For this reason, it will be important to understand the reconnection dynamics of such a configuration.

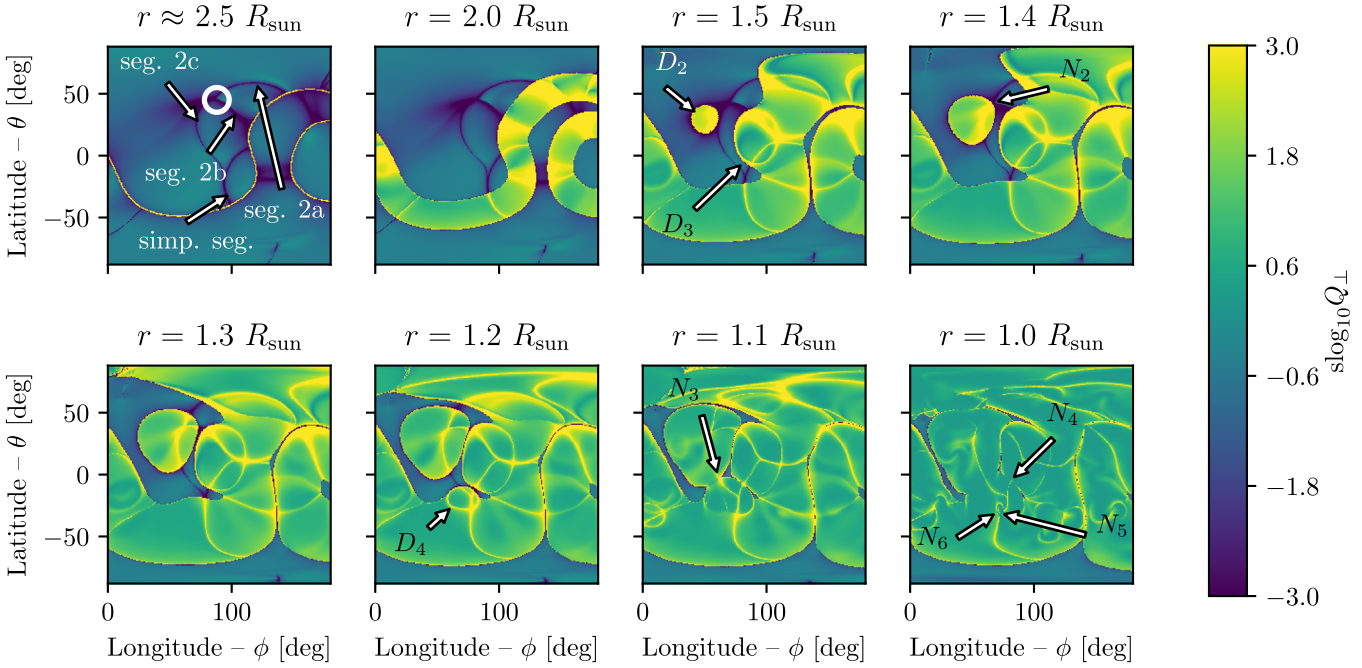

Figure 13. Perpendicular squashing factor ($\mathrm{slog}_{10} Q_\perp$) shown in eight slices of constant radius from photosphere to source surface. The domain is truncated to $\phi \in \{0°, 180°\}$ to focus on the system of branching segments with their vertex at $\theta \approx 40°$, $\phi \approx 90°$.

5. Observed S-Web Structures: Revisited

We have now established that HQA vertices are indicators of spine lines from magnetic nulls. Considering this, along with the narrowing of corridors to zero width, we can now return to the global model and interpret the structures that we see there. To help test our hypotheses, we determined the number and location of the magnetic nulls in the domain using the trilinear method introduced by Haynes & Parnell (2007). Not all of the detected nulls are relevant to the following, and we suspect that there may be additional nulls that were not detected by the method; however, a truncated list of relevant entries is given in Table 1. Each of the listed nulls is depicted in Figure 13, with the exception of N_1, which is responsible for "vertex 1" in Figure 5.

Considering the vertex labeled "vertex 2" in Figure 5, we can now describe the formation of each of the three attached segments (2a, 2b, and 2c in the figure) as well as the simple segment that appears to merge with segment 2c near $\theta \approx -20°$. In Figure 13, the western hemisphere is shown at eight different radial slices. The same vertex is indicated by the white circle at $\theta \approx 45°$ and $\phi \approx 90°$ in the top left panel, and this is indicative of a null spine line associated with the closed field separatrix surface labeled D_2 at $\theta \approx 30°$ and $\phi \approx 50°$ in the $r = 1.5\ R_{\rm Sun}$ panel. The associated null, N_2, is depicted in the $r = 1.4\ R_{\rm Sun}$ panel. Two more relevant separatrix domes (labeled D_3 and D_4 in the $r = 1.5\ R_{\rm Sun}$ and $r = 1.2\ R_{\rm Sun}$ panels) can be seen in the closed field, under the helmet streamer, and these cause the OCB footprint to bulge toward the footprint of the D_2.

In the lower left two panels ($r = 1.3\ R_{\rm Sun}$ and $r = 1.2\ R_{\rm Sun}$), the closed field region has expanded significantly, and the lower two branching segments (2b and 2c), as well as the simple segment, can each be associated with corridors that span from D_2 to the closed field separatrix domes (D_3 and D_4), as in Figure 11. The simple segment is now clearly associated with a corridor bounded by D_3 and D_4, as in Figure 10. In the $r = 1.1\ R_{\rm Sun}$ panel, the domes connected by segment 2c have now merged at the location of N_3, much like the triple-null configuration in Figure 11, and we now identify this segment as the footprint of a genuine separatrix curtain, which connects to a null dome composed of nulls N_2, N_3, and one or both of N_5 and N_6. The latter two nulls are visible in the bottom right ($r = 1.0\ R_{\rm Sun}$) panel of Figure 13. We can also see from the bottom right panel that the coronal holes enclosed by segments 2a and 2b remain connected to the larger open flux domain through corridors of narrow but presumably nonzero width (although their exact width cannot be accurately resolved), so the example shown in Figure 11 would seem to be well representative of the system of branching segments that we have described.

We also note that the narrow corridor associated with the simple segment previously mentioned has vanished at the location of N_4 in the $r = 1.0\ R_{\rm Sun}$ panel, and the two distinct dome structures have seemingly been replaced by a structure similar to that described in Figure 10. The merging of separatrix domes at low coronal heights appears to be a generic feature; we find from inspection that the majority of seemingly distinct dome structures are, in fact, connected by an

Table 1
Abridged Null List for 2014 July 29 PFSS Model

#	ϕ [deg. lng.]	θ [deg. lat.]	r [$R_{\rm Sun}$]
N_1	259.736	63.497	1.534
N_2	66.427	41.487	1.402
N_3	61.440	−2.811	1.110
N_4	81.234	−5.863	1.028
N_5	72.475	−31.234	1.006
N_6	71.011	−29.899	1.005

Note. N_1 (not shown) is associated with "vertex 1" (see Figure 5). The remaining nulls are indicated in the various panels of Figure 13. N_1, N_2, N_3, and N_4 form a portion of the OCB, whereas N_5 and N_6 appear to be entirely in the closed field region.

archway (at near photospheric heights) to one or more adjacent domes. This increase in complexity near the photosphere is to be expected; as we have discussed, the introduction of new nulls can cause separatrix surfaces to become linked and their respective flux domains to merge. In addition, it has been shown that increased resolution in global models leads to an increasing number of nulls, particularly at radial heights that are comparable to or less than the length scale of the photospheric magnetic field (Longcope & Parnell 2008; Edwards & Parnell 2015). Nonetheless, the importance of the large-scale null topology within the helmet streamer should not be underestimated, because it could have a significant effect on rates of reconnection at the OCB, thereby influencing IR processes.

6. Discussion

The aim of this investigation has been to better understand the origin of high-Q arcs within the S-Web in global coronal field extrapolations through comparison with generic model configurations of narrow corridors and magnetic null topologies. To this end, we have shown, using the popular PFSS coronal field model, that simple arcs that meet with the HCS at both ends tend to be good indicators of narrow coronal hole corridors, as per Antiochos et al. (2011). By contrast, branching structures with vertices that occur away from the HCS require a null spine line that emanates from a null dome structure in the open field and are, therefore, good indicators of more-complex magnetic topologies, such as those discussed in Platten et al. (2014). We also have seen that the distinction between these two regimes is largely a matter of where the nulls are positioned (because even the simpler corridor picture is likely to involve null dome structures in the closed field region), but that the likelihood of each occurring depends on the concave or convex nature of the nearby HCS.

This work supports the theory that S-Web arcs are likely to be locations where slow solar wind is observed. In particular, the implications of this study are pertinent to understanding IR and its role in the acceleration and structuring of the slow solar wind. Where IR involves flux that is bounded only by the global helmet streamer, the composition of the slow solar wind would involve plasma that formerly occupied a large coronal volume, out to a few solar radii; however, if volumes associated with low-lying null dome structures participate, then the exchange is likely to occur between open flux and dense plasma from the low corona, such as near active regions.

This distinction can be important both for the details of the reconnection process and for the composition of the material that is exchanged. The presence of these nulls may serve to increase both the rate of reconnection and the number of sites that could potentially host IR processes, increasing the likelihood that the S-Web can account for the amount of slow solar wind observed in situ. We have shown here that the location of coronal nulls, especially those associated with parasitic polarity regions embedded in otherwise open flux domains, can be inferred from the structuring of high-Q arcs, although the potential for simple arc segments to host unresolved null structures at very low heights must be studied in more detail. We submit, therefore, that the detailed dynamics and broad variability in the composition of the slow solar wind could be directly related to, and potentially inferred from, the distribution of these arc types in the heliosphere.

The complex connections that we have described here, particularly between branching arc segments and their connections across the OCB into the closed field regions, also have important implications for observations of impulsive SEP events. The unexpectedly wide longitudinal distributions of some impulsive SEP events could be due to the connections of magnetic field lines near the acceleration regions, particularly in configurations such as that depicted in Figure 11. Continuing with the example, if a flare event takes place deep within the closed field region, near the inner spine line of the lime green null, flare-accelerated particles would have easy access to the entire yellow arc segment, out to the orange vertex. Depending on the width of the dark green and purple coronal hole corridors, it is then easy to see how these particles may also have access to the corresponding S-Web arcs, thereby distributing flare-accelerated particles through a much larger portion of the heliosphere than is suggested by the compactness of the source.

In future work, we intend to extend this study through the consideration of the full 3D structure of the S-Web in global models, as well as the extension of our survey to a greater number of model cases, for both potential and, more generically, nonlinear force-free fields, for which the underlying magnetic topology is expected to be significantly more complex, as discussed by Edwards et al. (2015). To this end, we have developed a segmentation technique whereby the squashing factor is used to divide the coronal volume into flux domains, with high-Q volumes (being a combination of QSLs and separatrix surfaces) then recovered as the interfaces between these domains. In this way, arc vertices, which are the imprints of intersecting separatrix surfaces and QSLs, can be extracted automatically, and the corresponding volumes can be inspected for the existence of magnetic nulls and other topological features.

This work uses data obtained by the Global Oscillation Network Group program, managed by the National Solar Observatory, which is operated by AURA, Inc. under a cooperative agreement with the National Science Foundation. The data were acquired by instruments operated by the Big Bear Solar Observatory, High Altitude Observatory, Learmonth Solar Observatory, Udaipur Solar Observatory, Instituto de Astrofsica de Canarias, and Cerro Tololo Interamerican Observatory. We thank our colleagues in the Heliophysics Science Division at NASA Goddard Space Flight Center for their contributions to this effort. We also thank the anonymous referee for careful reading and helpful comments. Funding for this work has been provided through the UK's STFC under grants No. ST/N000714 and No. ST/N000781. P.F.W. is supported through the award of a Royal Astronomical Society Fellowship.

ORCID iDs

Roger B. Scott https://orcid.org/0000-0001-8517-4920
David I. Pontin https://orcid.org/0000-0002-1089-9270
Anthony R. Yeates https://orcid.org/0000-0002-2728-4053
Peter F. Wyper https://orcid.org/0000-0002-6442-7818
Aleida K. Higginson https://orcid.org/0000-0003-1380-8722

References

Antiochos, S. K., Mikić, Z., Titov, V. S., Lionello, R., & Linker, J. A. 2011, ApJ, 731, 112
Baker, D., Janvier, M., Démoulin, P., & Mandrini, C. H. 2017, SoPh, 292, 46

Brooks, D. H., Ugarte-Urra, I., & Warren, H. P. 2015, NatCo, 6, 5947
Cook, G. R., Mackay, D. H., & Nandy, D. 2009, ApJ, 704, 1021
Crooker, N. U., Antiochos, S. K., Zhao, X., & Neugebauer, M. 2012, JGRA, 117, A04104
Crooker, N. U., Gosling, J. T., & Kahler, S. W. 2002, JGRA, 107, 1028
Edmondson, J. K., Antiochos, S. K., DeVore, C. R., Lynch, B. J., & Zurbuchen, T. H. 2010, ApJ, 714, 517
Edwards, S. J., & Parnell, C. E. 2015, SoPh, 290, 2055
Edwards, S. J., Yeates, A. R., Bocquet, F. X., & Mackay, D. H. 2015, SoPh, 290, 2791
Freed, M. S., Longcope, D. W., & McKenzie, D. E. 2015, SoPh, 290, 467
Fujiki, K., Tokumaru, M., Hayashi, K., Satonaka, D., & Hakamada, K. 2016, ApJL, 827, L41
Giacalone, J., & Jokipii, J. R. 2012, ApJL, 751, L33
Gopalswamy, N., Yashiro, S., & Akiyama, S. 2016, ApJL, 823, L15
Haynes, A. L., & Parnell, C. E. 2007, PhPl, 14, 082107
Haynes, A. L., & Parnell, C. E. 2010, PhPl, 17, 092903
Higginson, A. K., Antiochos, S. K., DeVore, C. R., Wyper, P. F., & Zurbuchen, T. H. 2017a, ApJ, 837, 113
Higginson, A. K., Antiochos, S. K., DeVore, C. R., Wyper, P. F., & Zurbuchen, T. H. 2017b, ApJL, 840, L10
Li, C., Dai, Y., Vial, J. C., et al. 2009, A&A, 503, 1013
Longcope, D. W., & Parnell, C. E. 2008, SoPh, 254, 51
Longcope, D. W., & Parnell, C. E. 2009, SoPh, 254, 51
Masson, S., Antiochos, S. K., & DeVore, C. R. 2013, ApJ, 771, 82
Masson, S., Klein, K. L., Bütikofer, R., et al. 2009, SoPh, 257, 305
McCracken, K. G., Moraal, H., & Shea, M. A. 2012, ApJ, 761, 101
Owens, M. J., Crooker, N. U., & Lockwood, M. 2013, JGRA, 118, 1868
Owens, M. J., Crooker, N. U., & Lockwood, M. 2014, JGRA, 119, 36
Parenti, S., del Zanna, G., Petralia, A., et al. 2017, ApJ, 846, 25
Pariat, E., & Démoulin, P. 2012, A&A, 541, A78
Platten, S. J., Parnell, C. E., Haynes, A. L., Priest, E. R., & Mackay, D. H. 2014, A&A, 565, A44
Pontin, D. I., Bhattacharjee, A., & Galsgaard, K. 2007, PhPl, 14, 052106
Pontin, D. I., Priest, E. R., & Galsgaard, K. 2013, ApJ, 774, 154
Priest, E. R., & Démoulin, P. 1995, JGR, 100, 23443
Priest, E. R., Lonie, D. P., & Titov, V. S. 1996, JPlPh, 56, 507
Reames, D. V. 1999, SSRv, 90, 413
Savcheva, A. S., van Ballegooijen, A. A., & DeLuca, E. E. 2011, ApJ, 744, 78
Scott, R. B., Pontin, D. I., & Hornig, G. 2017, ApJ, 848, 117
Tassev, S., & Savcheva, A. 2017, ApJ, 840, 0
Titov, V. S. 2007, ApJ, 660, 863
Titov, V. S., Hornig, G., & Démoulin, P. 2002, JGRA, 107, 1164
Titov, V. S., Mikić, Z., Linker, J. A., Lionello, R., & Antiochos, S. K. 2011, ApJ, 731, 111
van Ballegooijen, A. A., Priest, E. R., & Mackay, D. H. 2000, ApJ, 539, 983
van Driel-Gesztelyi, L., Culhane, J. L., Baker, D., et al. 2012, SoPh, 281, 237
Wang, Y. M., Sheeley, N. R. J., & Rich, N. B. 2007, ApJ, 658, 1340
Wibberenz, G., & Cane, H. V. 2006, ApJ, 650, 1199
Wiedenbeck, M. E., Mason, G. M., Cohen, C. M. S., et al. 2013, ApJ, 762, 54
Yeates, A. 2018, antyeates1983/pfss: First release of pfss code, v1.0, Zenodo, doi:10.5281/zenodo.1472183